Indian Journal of Chemistry
Vol. 61, August 2022, pp. 878-894
DOI: 10.56042/ijc.v61i8.65054

Structural, spectral, bioactivity, antioxidant and molecular docking (with SARS-CoV-2) analyses on a new synthesized thiosemicarbazide derivative

Aytaç Güder*[a],Nuri Öztürk[b], Can Alaşalvar[c], Halil Gökce[a], Emre Menteşe[d], Hakan Bektaş[e]& Canan Albay[e]

[a] Giresun University, Vocational School of Health Services, 28100, Giresun, Turkey
[b] Giresun University, Dereli Vocational School, 28900, Giresun, Turkey
[c] Giresun University, Technical Science Vocational High School, 28100, Giresun, Turkey
[d] Recep Tayyip Erdogan University, Art and Science Faculty, 53100, Rize, Turkey
[e] Giresun University, Faculty of Art and Science, 28100, Giresun, Turkey

E-mail: aytac.guder@giresun.edu.tr

Received 12 November 2021; accepted (revised) 5 July 2022

Spectroscopic characterization of the N'-(4-nitrophenylcarbonothioyl) nicotinohydrazide molecule has been studied using both experimental (X-ray diffraction and IR spectroscopy) and quantum mechanical methods. The tautomeric energetic analysis, structural optimization parameters (bond lengths and angles), vibrational wave numbers, UV-Vis. parameters, the highest occupied molecular orbital (HOMO) and lowest unoccupied molecular orbital (LUMO) analyses and Molecular Electrostatic Potential (MEP) surface have been calculated by using DFT/B3LYP method with 6-311++G(2d,2p) level of theory to compare with the experimental results. The radical scavenging activity of the synthesized new compound has been evaluated using three different test methods. For this purpose, 2,2'-azino-bis-(3- ethylbenzothiazoline-6-sulfonate) (ABTS), *N*,*N*-dimethyl-*p*-phenylenediamine (DMPD) and 2,2-diphenyl-1-picrylhydrazyl (DPPH) radical scavenging activity tests has been done. The pharmacokinetic, physicochemical, and toxicity properties have been defined by using drug-likeness and *in silico* ADMET studies. The interaction characterization with SARS-CoV-2 main protease (M^{pro}) of the title compound has been investigated *via* the help of a molecular docking study.

Keywords: Bioactivity, antioxidant, molecular docking, SARS-CoV-2, thiosemicarbazide

Thiourea derivatives are chemically and biologically important organic reagents. In recent years, many substituted thiourea compounds have been synthesized and widely used in analytical chemistry[1-4]. Complexes of thiosemicarbazides, thiosemicarbazones, and dithiocarbazones have significant biological activity[5] and medicinal properties[6], especially according to the chemical structure of the part bound to the C=S carbon atom. The conjugated N-N-S ligand system of thiosemicarbazide is very useful in the synthesis of both organic and metal-organic compounds and these compounds have a very important place in the industry and medicinal chemistry. The importance of the compounds in this group is mainly due to their antimicrobial activities[7-10]. Thiosemicarbazide compounds exhibit various biological activities such as antifungal[10,11], kinase inhibitor[12], antioxidant[13,14], analgesic[15], anti-inflammatory[15], anticonvulsant[16,17], antidepressant[18], and as well as antitumor[19], antibacterial[20], and antiviral[20].Therefore, there are many papers in the literature on their pharmacological and biological properties such as antibacterial and antiproliferative activity, antifungal and antioxidant activity, biological activity, and molecular docking study[11-25].Besides these, thiosemicarbazides, which have remarkable properties, have been the subject of numerous coordination chemical studies. Many studies have been conducted on transition metal complexes of substituted thiosemicarbazides[7,8,26,27]. Coordination of these compounds with different metal ions often increases their activity[28]. Moreover, thiosemicarbazides have been widely used commercially as dyes, photographic films, plastic, and in the textile industry[29].On the other hand, a lot of scientists have been investigated the synthesis, structure and spectroscopic characterization of compounds including the thiosemicarbazide group as experimentally and theoretically[30-32].

In this study, we investigated the structure of a newly synthesized thiosemicarbazide derivative, N'-(4-nitrophenylcarbonothioyl) nicotinohydrazide molecule. The compound has been characterized

experimentally by using the single crystal X-ray diffraction and FT-IR spectroscopic techniques. We have been used DFT/B3LYP method with 6-311++G(2d,2p) level of theory to support the experimental results. HOMO-LUMO energies, electrical structural properties, and Molecular Electrostatic Potential map of the molecule have been examined by using the same method and level of theory.

In addition to the studies conducted, 2,2′-azino-bis (3-ethylbenzthiazoline-6-sulfonic acid) ($ABTS^{\bullet+}$), *N*,*N*-dimethyl-*p*-phenylenediamine ($DMPD^{\bullet+}$) and 2,2-diphenyl-1-picryl-hydrazyl ($DPPH^{\bullet}$) scavenging activity experiments have been performed.

Today, the search for effective chemical agents to combat with the Covid-19 virus and the effect on this virus of newly synthesized molecular compounds rapidly continues. With molecular docking analysis in this study, it was aimed to investigate the presence, nature and species of inter-molecular interactions between the synthesized thiosemicarbazide derivative crystalline compound and SARS-CoV-2 main protease (M^{pro}) protein (PDB ID: 6M0K).

Experimental Section

Synthesis of the N'-(4-nitrophenylcarbonothioyl) nicotinohydrazide

A mixture of nicotinic hydrazide (0.01 mol) and 4-nitrophenyl isothiocyanate (0.01 mol) in ethanol (20 mL) was refluxed for 4 hours. The end of the reaction was monitored by TLC (ethyl acetate/hexane= 2:1). Then, the mixture was cooled to RT and the product was observed by the addition of water. It was filtrated off, dried, and recrystallized.

Measurements

The single crystal data (CCDC number: 2077288) of the title compound have been recorded using Agilent SuperNova diffractometer with an Eos CCD detector (λ=0.71073 Å, T=298 K, MoKα radiation). CrysAlisPro software has been used for data collection, cell refinement, and data reduction[33]. SHELXS-2008[34]has been used to solve the crystallographic data and SHELXL-2015[35] program has been used to refine data. The molecular graphics have been visualized by using Olex 2 and Mercury program packages[36, 37]. Infrared spectrum of the compound in the solid state has been recorded at RT by using JASCO FT/IR-6600 Fourier Transform Infrared Spectrometer. The spectral range, resolution, and scan number for the IR spectrum were 4000-400 cm^{-1}, 1 cm^{-1}, and 16, respectively.

Determination of Free Radical Scavenging Activities

$ABTS^{\bullet+}$ Scavenging Activity Assay

The ABTS radical cation scavenging activity of the synthesized compound has been carried out with minor modifications on the performed method in the literature[38]. The basis of this method is based on the ability of antioxidants to remove stable blue / green color of ABTS radical cation with characteristic absorption at 734 nm. For this reason, ABTS radical cation has been formed by mixing 2.0 mmol/L ABTS and 2.45 mmol/L potassium persulfate. The radical cation solution formed has been kept in a dark RT environment for 16 h and has been used within 2 days. Before the activity tests, the absorbance value of the ABTS radical cation solution has been adjusted to be 0.750 ± 0.020 at 734 nm using PBS (0.1 M *p*H 7.4). For activity experiments, ABTS radical cation solution (1.0 mL) has been mixed with 3.0 mL of different concentrations (1-100 µg/mL) of the title compound prepared in PBS or solutions of standard substances. The results are expressed as the SC50 value obtained using linear regression analysis of absorbance values measured at four different concentrations three times.

$DMPD^{\bullet+}$ Scavenging Activity Assay

DMPD radical cation scavenging activity has been performed according to the spectrophotometric method frequently used in theliterature[39]. For this purpose, the DMPD radical cation solution at a concentration of 100 mM has been prepared. Taking 1 mL of this solution, acetate buffer (100 mL, 0.1 M, *p*H 5.25) has been added. DMPD radical cation has been obtained by adding 0.2 mL of ferric chloride solution (0.05 M) (final concentration was 0.01 mM). 225 µL of this solution has been taken and the absorbance value of the control tube has been recorded at 505 nm. To measure the activities of the title compound and standards at different concentrations (1-100 µg/mL), 15 µL has been taken and mixed with DMPD radical cation solution (210 µL). All tubes have been mixed on the vortex and incubated for 10 min. At the end of this period, the absorbance values of all tubes have been measured at 505 nm. In this assay, the decrease in the absorbance value is an indicator of the increase in activity. The buffer solution has been used as the

blank sample in this experiment. Experiments and calculations have been made as specified in ABTS radical cation.

DPPH•Scavenging Activity Assay

DPPH radical scavenging activity of the newly synthesized compound has been carried out following the spectrophotometric method, which is frequently used in the literature and is very useful in determining the activity indicator[40]. For this purpose, samples of the compound and the standard diluted at different concentrations (1-100 µg/mL) have been prepared. 200 µL of the prepared solution has been mixed DPPH• (2.8 mL, 0.2 mM) solution prepared in ethanol. The mixtures have been shaken on a vortex device for 15 s and incubated for 30 min at RT in the dark. For the activity calculations, the absorbance values of the samples in the tubes at 517 nm have been recorded. Experiments and calculations have been made as specified in ABTS radical cation.

Statistical analysis

Experimental results are shown as the mean ± S.D of three measurements. The analysis of variance has been performed by the ANOVA procedure. Significant differences between means have been determined by Duncan's Multiple Range tests. $P< 0.05$ has been considered significant. These operations have been done with the SPSS program (version 15.0.0; SPSS Inc., Chicago, IL, USA).

Computational Details

The geometry optimizations, vibrational wave-numbers, NMR chemical shifts, UV-Vis. spectroscopic parameters, HOMO-LUMO, and MEP analyses of the title compound have been computed using the Gaussian 09W program package[41]. The visualizations of calculated results have been performed by GaussView5.0 graphical interface program[42]. The molecular structures of six tautomers have been optimized at the B3LYP/6-311++G(2d,2p) level of theory. In DFT calculation, hybrid functional has been also used, the Becke's three parameter functional (B3)[43] which defines the exchange functional as the linear combination of Hartree-Fock, local and gradient corrected exchange terms. The B3 hybrid functional has been used in combination with the correlation functional of Lee, Yang and Parr[44].The vibrational wave-numbers of the compound have been computed based on the optimized molecular structure of the Tautomer 1 (thione-keto form) in the gas phase by using the B3LYP/6-311++G(2d,2p) level of theory. The fundamental vibrational band assignments have been performed in terms of Potential Energy Distribution (PED) by using the VEDA 4 program[45]. The UV-Vis. electronic absorption wavelengths have been calculated with time-dependent DFT (TD-DFT) method[46] by starting the optimized molecular structure in DMSO. The frontier molecular orbitals analyses have been simulated to identify the electronic transitions and charge transfers in the compound. Similarly, the MEP surface has been simulated using the optimized molecular geometry of the Tautomer 1 in a vacuum. To determine intermolecular interactions between the target macromolecule and the compound, the molecular docking study has been carried out by the AutoDock Vina program suite[47].

Results and Discussions

Crystallographic and optimized structure

The studied molecule has been crystallized in monoclinic system space group Pc with one isolated molecule in the asymmetric unit cell at the room-temperature. The data collection conditions and parameters of the refinement process have been summarized in Table I.

The crystal has been stabilized by six intermolecular interactions. On the other hand, no intramolecular hydrogen bond has been observed in the molecule. The interaction parameters have been listed in Table II and strong intermolecular interactions visualized in Figure 1. According to Table II, N4–H4···O3 interaction is stronger than the others. Other interactions may be considered short intermolecular interactions. The structural parameters of the N4–H4···O3 interaction have been observed as 0.86Å for N4-H4 distance, 1.97 Å (5) for H4$^{\cdots}$O^{ii}, 2.798 Å (5) and 161°for N4–H4···O3 angle.

The title compound has been optimized to compare X-ray results by using B3LYP level with 6-311G++(2d,2p) basis set. The molecular structure of the crystal has been shown in Figure 2. Moreover, the experimental and computed geometric parameters (bond lengths and angles) have been listed in Table III.

The C7-N3 and C7-N4 bond lengths have been observed as 1.335(6) Å and 1.370(5) Å and these bond lengths have been calculated as 1.362 Å and 1.377 Å, respectively. These values show that both bonds have a single bond character. On the other

Table I — Crystal data, data collection and refinement details of the compound (T1)

Chemical formula	$C_{13}H_{11}N_5O_3S$
Formula weight	317.33
Temperature (K)	293
Radiation type, Wavelength (Å)	Mo $K_{\acute{a}}$, 0.71073
Crystal system, Space group	Monoclinix, Pc
Unit cell parameters (), (°)	
a (Å)	8.6396 (5)
b (Å)	9.7716 (4)
c (Å)	8.1380(3)
â (°)	97.682°(5)
Volume (Å^3)	680.87 (5)
Z	2
Calculated density (mg cm^{-3})	1.548
ì (mm^{-1})	0.26
F_{000}	328
Crystal shape, color	Prism, colorless
Crystal size (mm)	0.2 × 0.15 × 0.1
è Ranges (°)	4.2 - 26.8
Index ranges	−10 ≤ h ≤ 10 −12 ≤ k ≤ 12 −10 ≤ l ≤ 10
No. of measured reflection, independent and observed [I>2σ(I)] reflection	8361, 2697 and 2416
Diffractometer	SuperNova, Single source at offset, Eos Diffractometer
Absorption correction	multi-scan
T_{min}, T_{max}	0.788, 1.00
Reflections, restraint, parameters	2697, 2, 200
R_{int}	0.034
Goodness-of-fit on F^2	1.08
Final R indices [F^2>2σ(F^2)]	0.045
*w*R(F^2)	0.112
$\Delta\rho_{max}$, $\Delta\rho_{min}$ (e Å^{-3})	0.38, -0.18
Weighting scheme	$w = 1/[\sigma^2(F_o^2) + (0.0639P)^2 + 0.0456P]$ $P = (F_o^2 + 2F_c^2)/3$

Table II — Hydrogen bond geometryparameters (Å, °) of the compound (T1)

D–H···A	D-H	H···A	D···A	D-H···A
N2-H2···N1^{i}	0.86	2.14	2.951 (5)	158
N4-H4···O3^{ii}	0.86	1.97	2.798 (5)	161
N3-H3···O3^{ii}	0.86	2.40	3.121 (5)	141
N3-H3···O3^{iii}	0.86	2.81	3.343 (6)	122
C3-H3A···O3^{iv}	0.93	2.51	3.401 (6)	160
C1-H1···O1^{v}	0.93	2.71	3.397 (6)	132

(i) x-1, y, z-1; (ii) x, -y, z+1/2; (iii) x-1, y, z-1; (iv) x-1, -y, z-3/2; (v) x-1, y, z-2

hand, the C7–S1 and C6–O3bond lengths have been found as 1.655(5) Å – 1.237 Å (5) (exp.) and 1.670 Å −1.227 Å (comp.). Thus, it can be said that these bonds have a double bond character. Torsion angles

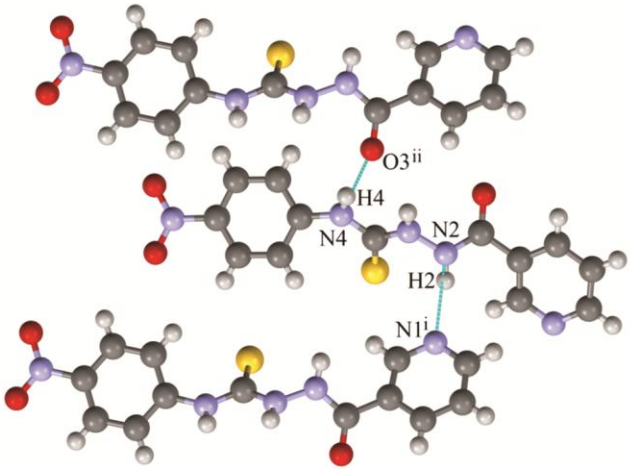

Figure 1 — Strong intermolecular interactions of the compound

(C4-C6-N2-N3, C6-N2-N3-C7, N2-N3-C7-N4, N3-C7-N4-C8) in the thiosemicarbazide chain have been obtained as 175.1° (4), 125.4° (5), 177.1°(4), −172.5° (4) (exp.) and 175.9°, −150.8°, 179.4° and −173.2° (comp.) respectively. The information obtained from the X-ray results proves that the tautomeric form of the molecule is the thione-keto form.

Different tautomeric forms can arise with the displacement of protons in the thiosemicarbazide chain. Possible tautomeric forms of the molecule have been optimized to investigate the tautomeric analysis of the structure. Six different tautomeric forms of the structure have been demonstrated in Figure 3 and bond parameters on the thiosemicarbazide chain have been given in Table IV. Looking at Table IV, it is seen that the bond characters change in different tautomeric situations. For example, in the thione-enol(T4) form, while the C6-N2 and C7-S1 bonds are double bonds, the C6-O3, N2-N3, C7-N3, and C7-N4 bonds have single bond character. On the other hand, The C6-O3 and C7-N3 bonds have double bond character and the C6-N2, N2-N3, C7-N4, and C7-S1 bonds are single bonds in the thiol-keto (T2) form.

Moreover, when the energy value of the thione-keto form (T1)of the compound has taken 0 kcal/mol, relative energies for other forms have been found as 8.609 kcal/mol (thiol-keto form (T2)), 12.159 kcal/mol (thiol-keto form(T3)), 13.439 kcal/mol (thione-enol form (T4)), 15.784 kcal/mol (thiol-enol form (T5)) and 19.866 kcal/mol (thiol-enol form(T6)). Looking at the energy values in Figure 3, it can be said that the most stable form is the thione-keto form. These data obtained from the DFT calculations support the X-ray analysis results.

Table III — The measured and calculated molecular geometry parameters of compound (T1)

Bondlengths (Å)	Exp.	Calc.	Bondangles (°)	Exp.	Calc.	Bondangles (°)	Exp.	Calc.
C7-S1	1.655(5)	1.670	H2-N2-N3	120.2	111.9	C4-C3-C2	118.5(4)	118.8
C6-O3	1.237(5)	1.227	H2-N2-C6	120.2	124.6	H3A-C3-C2	120.7	121.9
N2-H2	0.860	1.017	N3-N2-C6	119.7(3)	115.7	C11-C10-H10	120.5	119.8
N2-N3	1.391(5)	1.386	H4-N4-C7	115.9	114.6	C11-C10-C9	118.9(4)	118.9
C6-N2	1.326(5)	1.369	H4-N4-C8	128.2(4)	113.7	H10-C10-C9	120.5	121.3
N5-O2	1.230(5)	1.227	C7-N4-C8	115.9	131.1	N4-C8-C9	122.4(4)	116.6
N5-O1	1.221(5)	1.226	O2-N5-O1	118.6(4)	124.5	N4-C8-C13	117.9(4)	123.9
N4-H4	0.860	1.009	O2-N5-C11	122.5(4)	117.7	C9-C8-C13	119.5(4)	119.4
C7-N4	1.370(5)	1.377	O1-N5-C11	118.9(4)	117.8	C10-C9-C8	120.4(4)	120.8
C8-N4	1.398(5)	1.403	C5-N1-C1	116.9(4)	117.6	C10-C9-H9	119.8	119.4
C11-N5	1.458(6)	1.467	N2-N3-H3	119.6	110.2	C8-C9-H9	119.8	119.7
C5-N1	1.339(6)	1.332	N2-N3-C7	120.7(4)	120.1	C8-C13-H13	120.0	120.2
C1-N1	1.332(6)	1.335	H3-N3-C7	119.6	122.8	C8-C13-C12	119.9(4)	119.8
N3-H3	0.860	1.016	C6-C4-C3	118.4(4)	118.4	H13-C13-C12	120.0	120.0
C7-N3	1.335(6)	1.362	C6-C4-C5	118.8(4)	123.5	N1-C5-C4	123.2(4)	123.5
C4-C6	1.503(6)	1.488	C3-C4-C5	122.8(4)	118.1	N1-C5-H5	118.4	115.6
C4-C3	1.384(6)	1.395	S1-C7-N4	125(3)	127.1	C4-C5-H5	118.4	120.8
C4-C5	1.384(6)	1.398	S1-C7-N3	122.9(3)	121.9	C11-C12-C13	120.1	119.9
C11-C10	1.378(6)	1.389	N4-C7-N3	112.1(4)	110.9	C11-C12-H12	119.8(4)	119.5
C11-C12	1.376(6)	1.389	O3-C6-N2	123.7(4)	120.4	C13-C12-H12	120.1	120.7
C3-H3A	0.930	1.080	O3-C6-C4	120.6(4)	123.3	N1-C1-H1	118.1	116.1
C3-C2	1.377(7)	1.385	N2-C6-C4	115.5(3)	116.4	N1-C1-C2	123.9(4)	123.4
C10-H10	0.930	1.078	N5-C11-C10	119.6(4)	119.3	H1-C1-C2	118.1	120.5
C10-C9	1.379(6)	1.381	N5-C11-C12	118.9(4)	119.5	C3-C2-C1	118.6(4)	118.6
C8-C9	1.385(6)	1.403	C10-C11-C12	121.4(4)	121.2	C3-C2-H2A	120.7	121.1
C8-C13	1.400(6)	1.399	C4-C3-H3A	120.7	119.3	C1-C2-H2A	120.7	120.3
C9-H9	0.930	1.082	–	–	–	–	–	–
C13-H13	0.930	1.076	–	–	–	–	–	–
C13-C12	1.366(6)	1.385	–	–	–	–	–	–
C5-H5	0.930	1.084	–	–	–	–	–	–
C12-H12	0.930	1.078	–	–	–	–	–	–
C1-H1	0.930	1.083	–	–	–	–	–	–
C1-C2	1.382(7)	1.392	–	–	–	–	–	–
C2-H2A	0.930	1.081	–	–	–	–	–	–

Table IV — Calculated bond lengths on the thiosemicarbazide chain of compounds

	T1	T2	T3	T4	T5	T6
C8-N4	1.402	1.389	1.399	1.398	1.385	1.394
C7-N4	1.376	1.265	1.392	1.385	1.275	1.386
C7-S1	1.670	1.796	1.805	1.651	1.795	1.786
C7-N3	1.362	1.395	1.276	1.379	1.371	1.285
N3-N2	1.386	1.390	1.358	1.356	1.354	1.380
C6-N2	1.369	1.389	1.382	1.276	1.277	1.281
C6-O3	1.227	1.215	1.213	1.373	1.370	1.356
C6-C4	1.488	1.493	1.500	1.469	1.469	1.476

FT-IR analysis

The compound belonging to the C1 point group has 33 atoms and thus 93 (3N-6) vibration modes. Harmonic vibrational wave-numbers calculated with the B3LYP/6-311++G(2d,2p) level of theory have been scaled with 0.955 for the region between 4000-1700 cm^{-1} and 0.985 for the region below 1700 cm^{-1}.

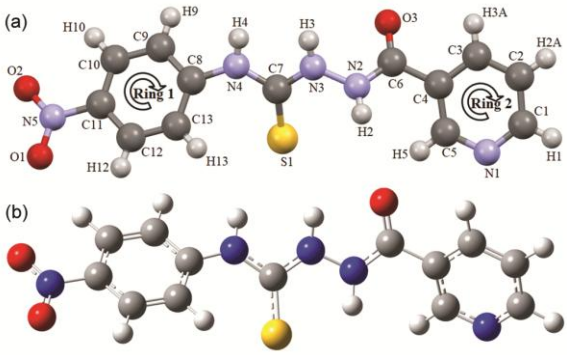

Figure 2 — The (a) experimental and (b) optimized molecular structure of the crystal

The vibrational band assignments, experimental frequencies, computed wave-numbers and IR intensities of the compound have been given in Table V. The experimental and computed IR spectra

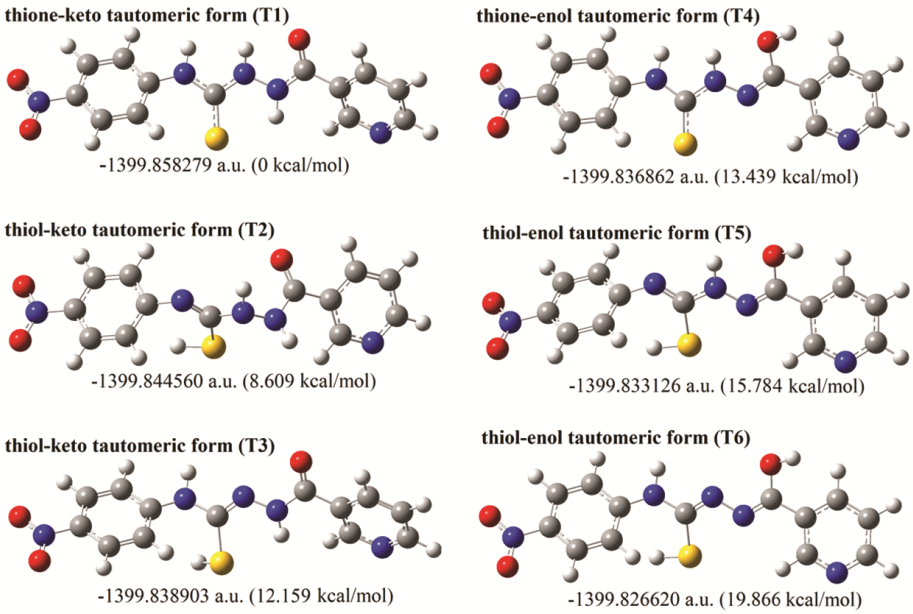

Figure 3 — Possible tautomeric forms of the molecule

Table V — The experimental and computed vibrational wave-numbers and their assignments of the compound (T1).

Assignments (PED%)	Exp.(cm^{-1})	Calculated		
		Unscaled	Scaled	I_{IR}
ν(N4-H4)(100)	3319 s	3581	3420	26.6
ν(N3-H3)(96)	3240 m	3501	3343	293.9
ν(N2-H2)(96)	3209 m	3456	3300	163.1
ν(CH)(93) in Ring1	3161 m	3248	3102	1.4
ν(CH)(98) in Ring1	-	3231	3086	3.3
ν(CH)(92) in Ring1	3085 s	3228	3083	2.7
ν(CH)(99) in Ring2	-	3209	3065	5.8
ν(CH)(95) in Ring2	3054 s	3194	3051	7.3
ν(CH)(99) in Ring1	-	3173	3030	7.4
ν(CH)(87) in Ring2	3026 sh	3164	3022	6.0
ν(CH)(93) in Ring2	-	3158	3016	18.7
Overtone or combination bands	2980 m 2918 m 2862 m 2814 m	–	–	–
ν(C=O)(76)	1663 vs	1694	1669	242.2
ν(CC)(40) in Ring1 + β(H4-N4-C8)(13)	–	1646	1621	40.4
[ν(CC)(49) + β(CCC)(10)] in Ring1	1616 s	1637	1612	180.0
[ν(CN)(22) + ν(CC)(27)] in Ring2	1596 vs	1628	1604	50.9
[ν(CC)(43) + β(CCC)(10) + β(HCN)(10)] in Ring2	–	1603	1579	3.7
β(H4-N4-C8)(45) + $\nu_{as}(NO_2)$(26)	1569 vs	1585	1561	354.8
β(H3-N3-N2)(33) + β(H2-N2-C6)(19)	1550 sh	1568	1545	32.3
$\nu_{as}(NO_2)$(49) + β(H4-N4-C8)(12)	1534 w	1550	1527	341.2
[β(HCC)(59) + ν(CC)(12)] in Ring1	–	1533	1510	30.6
[β(HCC)(25) + β(HCN)(20) + ν(CC)(11)] in Ring2	1497 vs	1516	1494	18.7
β(HCN)(41) in Ring2	1451 sh	1452	1430	48.1
[ν(CC)(39) + β(HCC)(12)] in Ring1	-	1451	1430	78.7
β(H3-N3-N2)(22) + β(H2-N2-C6)(19) + ν(C6-N2)(18)	1416 s	1429	1408	1103.0
[β(HCN)(40) + β(HCC)(23)] in Ring2	1360 w	1371	1351	5.4
$\nu_s(NO_2)$(46)	1340 vs	1368	1348	227.1

(*Contd.*)

Table V — The experimental and computed vibrational wave-numbers and their assignments of the compound (T1). (*Contd*.)

Assignments (PED%)	Exp.(cm^{-1})	Calculated		
		Unscaled	Scaled	I_{IR}
ν(CC)(53) in Ring1	–	1359	1338	251.6
β(HCC)(50) in Ring1 + $ν_s(NO_2)$(10)	1323 w	1348	1328	345.8
ν(C7-N4)(25) + ν(C8-N4)(13) + β(HCC)(23) in Ring1	–	1328	1308	635.4
ν(N3-N2)(21) + ν(C7-N3)(11) + β(H2-N2-C6)(11)	1300 m	1310	1291	7.6
[ν(CN)(51) + ν(CC)(15)] in Ring2	1256 s	1285	1266	1.5
β(H3-N3-N2)(16) + ν(C6-C4)(10)	–	1262	1243	139.5
ν(C8-N4)(16) + [β(CCC)(11) + ν(CC)(10)] in Ring1	1222 sh	1256	1237	135.7
[ν(CN)(20) + β(HCN)(20) + β(HCC)(16)] in Ring2	1203 m	1221	1203	7.5
[β(HCC)(57) + ν(CC)(12)] in Ring1	1194 sh	1208	1189	30.9
ν(NN)(25) + ν(C7-N4)(11) + ν(C7-N3)(10)	1174 m	1188	1170	79.8
[β(HCC)(67) + ν(CC)(22)] in Ring1	1125 sh	1140	1123	8.0
[β(HCC)(48) + ν(CC)(16)] in Ring2	–	1136	1119	17.0
ν(C11-N5)(20) + [ν(C10-C11)(33) + β(HCC)(17)] in Ring1	1109 s	1126	1109	135.7
ν(C6-N2)(23) + β(H2-N2-C6)(10)	1064 w	1113	1097	18.0
[ν(CC)(54) + ν(CN)(17)] in Ring2	1043 m	1060	1044	0.7
[β(CNC)(46) + β(CCC)(18) + β(NCC)(16)] in Ring2	1031 m	1043	1027	14.4
β(CCC)(93) in Ring1	1010 w	1029	1014	0.2
[τ(HCCN)(32) + τ(HCCC)(28) + τ(HCNC)(21) + τ(NCCC)(10)] in Ring2	995 w	1020	1005	1.3
[τ(HCCC)(74) + τ(CCCC)(17)] in Ring1	–	998	983	1.2
[τ(HCNC)(60) + τ(HCCC)(32)] in Ring2	973 w	994	979	0.5
[τ(HCCC)(47) + τ(CCCC)(13)] in Ring1 + τ(H9-C9-C8-N4)(25)	–	983	968	0.8
[τ(HCNC)(53) + τ(CNCC)(21)] in Ring2	944 w	955	941	1.8
β(OCN)(20) + β(N3-N2-C6)(11)	906 m	928	914	17.3
β(CCC)(13) in Ring1	879 m	888	874	41.3
τ(HCCC)(48) in Ring1 + τ(H9-C9-C8-N4)(20) + γ(OCON)(10)	852 m	867	854	30.1
$β(NO_2)$(40)	–	856	843	21.2
[τ(HCCN)(41) + τ(CCCC)(11)] in Ring2 + γ(ONCC)(12) + γ(CCCC)(10)	825 m	843	830	7.3
τ(H9-C9-C8-N4)(42) + τ(HCCC)(54) in Ring1	–	826	813	4.0
γ(OCON)(46) + τ(CCCC)(13) in Ring1	758 w	776	765	13.4
ν(CS)(22) + γ(O3-N2-C4-C6)(11)	738 s	749	738	17.8
γ(ONCC)(42)	–	746	734	41.0
β(NCC)(11) in Ring2	–	735	724	19.7
[τ(CCCC)(35) + τ(CNCC)(23) + τ(NCCC)(13) + τ(HCNC)(11)] in Ring2	715 s	722	711	18.4
τ(CCCC)(30) in Ring1	–	705	694	20.4
τ(CCCC)(36) in Ring1	688 w	693	683	6.2
ν(CS)(26) + β(C7-N3-N2)(12) + β(S1-C7-N3)(10)	664 m	657	648	11.7
β(CCC)(64) in Ring1	631 m	642	633	2.9
[β(CCC)(51) + β(CNC)(19)] in Ring2	621 sh	635	625	6.1
γ(SNNC)(72)	605 m	601	592	6.1
τ(H2-N2-C6-C4)(23) + τ(H3-N3-C7-N4)(11)	544 m	548	540	38.9
β(ONC)(47) + τ(H2-N2-C6-C4)(12) + β(N5-C11-C12)(10)	528 sh	532	524	16.6
β(N2-C6-C4)(22) + τ(H2-N2-C6-C4)(17)	512 vw	527	519	19.3
τ(H4-N4-C8-C9)(56)	–	511	504	45.8
τ(H4-N4-C8-C9)(21) + τ(CCCC)(33) in Ring1	493 m	488	480	130.8
τ(H3-N3-C7-N4)(40)	470 w	476	469	84.2
ν(C11-N5)(11)	448 sh	452	445	19.5
[τ(CCCC)(47) + τ(HCCC)(10)] in Ring1	424 w	425	418	0.5
τ(CCCC)(23) in Ring2	407 w	423	417	5.7

(*Contd*.)

Table V — The experimental and computed vibrational wave-numbers and their assignments of the compound (T1). (*Contd.*)

Assignments (PED%)	Exp.(cm^{-1})	Calculated		
		Unscaled	Scaled	I_{IR}
[τ(NCCC)(32) + τ(HCNC)(13)] in Ring2 + γ(CCCC)(13)	–	400	394	1.0
ν(C6-C4)(17) + ν(C11-N5)(10)	–	360	355	8.2
β(C13-C8-N4)(17) + β(OCN)(10)	–	352	346	3.0
β(N3-N2-C6)(17) + β(C6-C4-C5)(14) + β(OCN)(10)	–	314	309	60.8
γ(NCCC)(27) + τ(C12-C13-C8-N4)(25)	–	292	287	15.5
β(S1-C7-N3)(30) + τ(NNCC)(15)	–	274	270	3.7
β(N5-C11-C12)(36) + β(ONC)(11) + β(C8-N4-C7)(10)	–	225	221	1.4
β(C6-C4-C5)(19) + τ(NCNN)(12)	–	218	215	5.0
γ(CCCC)(23) + [τ(NCCC)(14) + τ(CNCC)(13)] in Ring2 + τ(NCNN)(13)	–	165	163	10.3
β(C8-N4-C7)(10)	–	157	155	4.2
γ(NCCC)(15) + β(N2-C6-C4)(12) + β(NCN)(12) + τ(CNCN)(11)	–	124	122	3.4
τ(CCNC)(18) + β(C13-C8-N4)(12)	–	99	98	2.3
τ(CNNC)(37) + τ(N2-C6-C4-C3)(37)	–	73	72	4.9
τ(ONCC)(29) + β(N2-C6-C4)(13) + β(N3-N2-C6)(13) + τ(NCNN)(11)	–	65	64	1.8
τ(ONCC)(62) + τ(NCNN)(10)	–	60	59	1.6
τ(CNCN)(23) + τ(NNCC)(13) + β(C7-N3-N2)(11) + τ(NCCC)(11)	–	35	35	1.3
τ(NCCC)(38) + τ(CNNC)(14) + τ(NNCC)(14)	–	31	30	1.1
τ(CNCN)(31) + τ(CNNC)(19) + τ(NCNN)(15) + τ(NNCC)(11)	–	16	16	0.4
τ(CCNC)(39) + β(C8-N4-C7)(17) + β(C13-C8-N4)(10) + τ(CNNC)(10)	–	13	13	0.2

ν, stretching; β, in-plane bending; τ, torsion; γ, out-of-plane bending; vs, very strong; s, strong; m, medium; w, weak; sh, shoulder; I_{IR}, IR intensity (km/mol); PED, potential energy distribution.

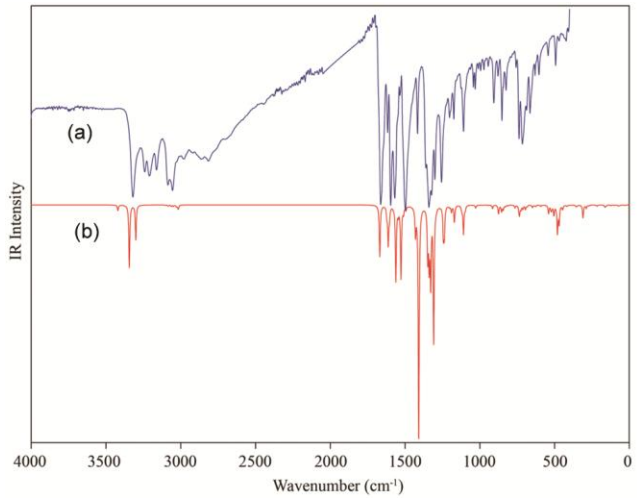

Figure 4 — The (a) experimental and (b) computed IR spectra of the compound

have been given in Figure 4. Linear correlation coefficient (R^2) and root mean square (RMS) values between the experimental frequencies and computed vibrational wave-numbers have been computed as 0.99917 and 26.17 cm^{-1}, respectively. The differences between the experimental and calculated vibrational bands are due to the using of the solid phase of the molecule has intermolecular interaction in the experimental measurement, while the isolated form of the molecule is used in theoretical calculation.

The N-H stretching bands without inter- and intramolecular hydrogen bond interactions give peaks at higher frequency regions (above 3200 cm^{-1}) of the vibrational spectrum[48-52]. However, under the effect of inter and intramolecular interactions, the position of these vibrational modes shift to lower frequency regions. Moreover, the NH bands under the effect of the strong hydrogen bond interaction are observed as a broad absorption band in the region of 3200-2400 cm^{-1} [48-51]. In the presence of intermolecular N2-H2···N1^{i} and N4-H4···O3^{ii} interactions obtained from X-ray diffraction, N-H stretching vibrations have been observed at 3319 cm^{-1}, 3240 cm^{-1} and 3209 cm^{-1} in the experimental IR spectrum. On the other hand, these vibration modes have been calculated at 3420 cm^{-1}, 3343 cm^{-1} and 3300 cm^{-1}, each in the frequency region approximately 100 cm^{-1} higher than the experimental frequencies. As mentioned, these frequency differences between the

experimental and computed NH stretching bands are due to the intensity of the intermolecular interactions. Moreover, HNC and HNN in-plane bending vibrations have been observed in the range of 1550-1064 cm^{-1} in the experimental IR spectrum, while they were calculated in the range of 1621-1097 cm^{-1} (with PED contributions between 52%-10%) in combination with other vibration modes in the fingerprint region of the IR spectrum. The C=O stretching vibration can be observed within the range of 1540-1870 cm^{-1} depending on the environmental factors blockading it. The recorded very strong absorption band at 1663 cm^{-1} in the IR spectrum and the computed wave-number value at 1669 cm^{-1} has been assigned to the C=O stretching bond[53, 54].

On the other hand, as seen in Table V, the stretching vibration bands of C7=S1 have been experimentally observed at 738 cm^{-1} and 664 cm^{-1}, while they have been calculated at 738 cm^{-1} and 648 cm^{-1}. There is no significant difference between the experimental and calculated C=S stretching vibration and they are in agreement with the literature[55-58].

The observed bands at the interval of 3161-3026 cm^{-1} have been assigned to the CH stretching modes in phenyl and pyridine rings, while these vibrational modes have been calculated in the region of 3102-3016 cm^{-1} for aromatic rings. The vibration bands observed in the experimental IR spectrum between 2980 cm^{-1} and 2814 cm^{-1} are overtone and combination bands.

The CC and CN stretching vibrations of the aromatic ring are located within region below 1650 cm^{-1} [48-51]. CC skeletal stretching vibrations in the phenyl and pyridine rings have been observed between 1616-1497 cm^{-1} in the experimental IR spectrum, while these modes have been computed in the region of 1621-1494 cm^{-1} [52, 59]. Other CC stretching vibrations in pyridine and nitrophenyl ring have been observed in the range of 1256-1043 cm^{-1}, while computed between 1451 cm^{-1} and 1044 cm^{-1}. The CC stretching vibration between the pyridine ring and the carbon atom at the end of the aliphatic chain has been calculated at 1243 (with PED contribution of 10%) cm^{-1} and 355 (with PED contribution of 17%) cm^{-1}. As can be seen from Table V, CN stretching vibrations in the pyridine rings have been observed at 1596 cm^{-1}, 1256 cm^{-1}, 1203 cm^{-1}, 1043 cm^{-1} and these bands have been computed at 1604 (PED-22%) cm^{-1}, 1266 (PED-51%) cm^{-1}, 1203 (PED-20%) cm^{-1}, 1044 (PED-17%) cm^{-1}. The bands located at 1109 (exp.)/1109 (PED-20%) cm^{-1}, 448 (exp.)/445 (PED-11%) cm^{-1} and 355 (PED-10%) cm^{-1} have been also assigned to the CN stretching vibration between the nitro group and the phenyl ring[48, 49, 51]. The other CN stretching vibrations in the aliphatic region have been observed between 1416-1064 cm^{-1} in the experimental IR spectrum and have been determined between 1408-1097 cm^{-1} with the computational level of theory. The NN stretching vibrations have been observed at 1300 cm^{-1} and 1174 cm^{-1} in the experimental IR spectrum and have been computed at 1291 (PED-21%) cm^{-1} and 1170 (PED-25%) cm^{-1}. If we consider NO_2 vibration modes, which is one of the important characteristic bands of the molecule, the bands located at 1569 (exp.)/1561 (PED-26%) cm^{-1} and 1534 (exp.)/1527 (PED-49%) cm^{-1} have been assigned to the asymmetric NO_2 stretching vibration, while the bands at 1340 (exp.)/1348 (PED-46%) cm^{-1} and 1323 (exp.)/1328 (PED-10%) cm^{-1} have been assigned to the symmetric NO_2 stretching vibration[60-62]. On the other hand, the in-plane bending vibration of the NO_2 band has been calculated at 843 (PED-40%) cm^{-1} with the computational level of theory. All other in-plane bending, out-of-plane bending and torsion vibration bands have been summarized in Table V. Based on the information obtained above, we can say that the tautomeric form of the molecule is in the thione-keto form according to the values of C-N, C=O, C=S, N-N, and N-H vibrational frequencies in the thiosemicarbazide chain.

HOMO, LUMO, and UV-Vis. analyses

To determine the intramolecular electronic transitions of the title molecule, UV-Vis. spectroscopic analyses have been carried out theoretically. UV-Vis. parameters (wavelengths, excitation energies, oscillator powers and electronic transitions) have been calculated at TD-DFT/B3LYP/6-311++G(2d,2p) level of theory in DMSO using the IEFPCM model. All spectroscopic parameters corresponding to the calculated wavelengths have been detailed in Table VI. The percentages of major contributions for electronic transitions corresponding to the calculated wavelengths given in Table VI have been investigated with Gauss Sum 3.0.1 program package[63]. Besides, the calculated UV-Vis. spectrum has been given in Figure 5.

As known, the highest occupied molecular orbital (HOMO) and the lowest unoccupied molecular orbital (LUMO), called frontier molecule orbitals (FMO), are used to determine electronic transitions, charge transfers and some other electronic features of molecules. HOMO orbitals are related to the

Table VI — The UV-Vis. spectral parameters of the compound (T1) in DMSO.

$ë_{calc.}$ (nm)	Ä*E* (eV)	*f*	Major contributions
399.94	3.1001	0.0204	H-1→L (71%), H→L (16%)
384.42	3.2252	0.1629	H→L (77%), H-1→L (21%)
374.11	3.3141	0.5988	H-2→L (87%)
326.53	3.7970	0.0039	H-8→L (95%)
314.45	3.9429	0.0027	H-1→L+1 (51%), H→L+1 (22%)
304.11	4.0770	0.2849	H→L+1 (69%), H-1→L+1 (27%)

Ä*E*, Excitation energy; *f*, Oscillator strengths

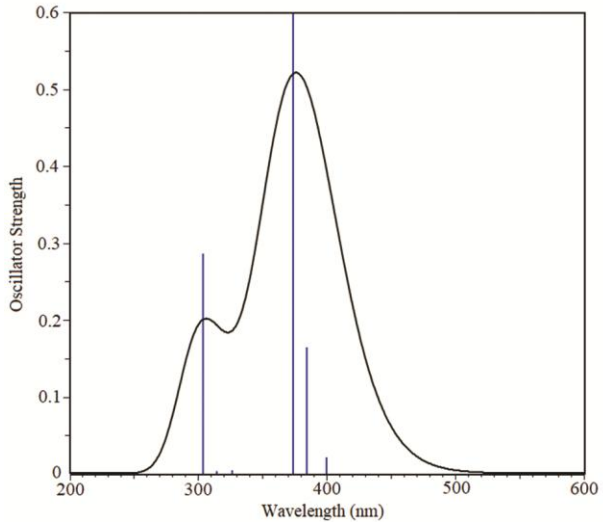

Figure 5 — The calculated UV-Vis. spectrum of the compound

ionization potential behaving as an electron donor, while LUMO orbitals are related to the electron affinity behaving as an electron acceptor. Moreover, the HOMO-LUMO band gap allows us to gain insight into the reactivity and chemical stability of molecules[64]. If a molecule has a small band gap, it qualifies as a soft molecule and is more polarizable and generally associated with high chemical reactivity[65,66]. HOMOs (H, H-1 and H-8) and LUMOs (L and L+1) simulated based on optimized molecular geometry in DMSO have been given in Figure 6. The green regions in the HOMOs and LUMOs given in the Figure 6 represent the negative phases and the red regions represent the positive phases.

The HOMO, LUMO, and |HOMO-LUMO| bandgap for title compound have been calculated as -6.666 eV, -3.047 eV, and 3.619 eV, respectively. As seen in Figure 6, HOMO-8 has almost entirely localized on the nitro group. HOMO-2 has mostly localized over lone pairs of the sulfur atom and partially over n orbitals of the nitrogen atom and bonding-π molecular orbitals within the nitrophenyl.HOMO-1 has mainly localized over lone pairs of the sulfur atom. HOMO has mostly concentrated on lone pairs of sulfur atoms and n orbitals of nitrogen atoms. The LUMO molecular orbital has distinctly formed from antibonding-π molecular orbitals of -C=C- group within the nitrophenyl and pyridine ring and lone pairs of the oxygen atoms of the nitro group. As the last one, LUMO+1 has mainly formed from antibonding-π molecular orbitals of the -C=C- group within the pyridine ring. When looking at the electron localizations of the compound on the HOMO and LUMO molecular orbitals given in Figure 6, it can be said that the electronic transitions are mostly n→π*. HOMO→LUMO (77%) transition corresponding to the computed wavelengths/oscillator strength at 384.42 nm/0.1629 by GaussSum can be attributed to n→π* electronic transition.

Also, H-1→L (71%), H-8→L (95%), H-1→L+1 (51%) H→L+1 (69%)transitions corresponding to the computed wavelengths/oscillator strength at 399.94 nm/0.0204, 326.53 nm/0.0039, 314.45 nm/0.0027 and 304.11 nm/0.2849, respectively, can be attributed to n→π* electronic transition. However, it is not differentiated whether the H-2→L (87%) transition corresponding to the computed wavelengths/oscillator strength at 374.11 nm/0.5988 isn→π* or π→π* electronic transition.

In addition, the ionization potential (*I*), electron affinity (*A*), electronegativity (χ), chemical hardness (η), softness (*S*), electrophilicity index (ω), and maximum charge transfer index ($\Delta N_{max.}$) calculated based on the energies of the HOMO and LUMO orbitals of the molecule have been listed in Table VII.

MEP surface analysis

As known, the electrostatic potential of a molecule is one of the most useful ways to evaluate the chemical reactivity of the molecule against negatively or positively charged reagents. In short, it is a very useful method for determining intramolecular and intermolecular interaction sites and hydrogen bonds. The values of the electrostatic potential on the surface

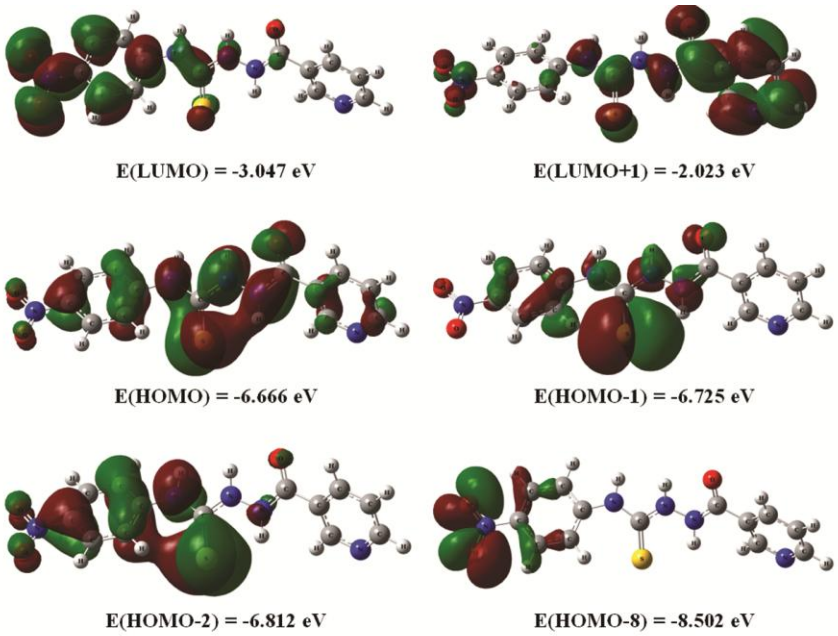

Figure 6 — The simulated HOMO-LUMO orbitals of the molecule

of a molecule are represented by different colors depending on the increase, namely red < orange < yellow < green < blue. The negative electrostatic potential regions appearing in red on the three-dimensional surface of the MEP are nucleophilic centers and the positive electrostatic regions appearing in blue are electrophilic centers. Nucleophilic centers are usually related to the lone pair of electronegative atoms while electrophilic centers are mostly localized on hydrogens. The MEP surfaces for both sides of the molecule calculated at the B3LYP/6-311++G(2d,2p) level of theory in the gas phase to determine the positive and negative electrostatic regions have been visualized in Figure 7.

As can be seen in Figure 7, the positive regions on the MEP surface of the compound have mainly localized on hydrogen atoms and especially on the H4 atom with a positive electrostatic potential value of +0.07843.Wecan understand that there may be intermolecular hydrogen bonding from the concentration of the dark blue area on the MEP surface on the H4 hydrogen atom. On the other hand, negative regions have localized, as expected, especially at sulfur, oxygen and nitrogen atoms. The most negative electrostatic regions on the MEP surface have been calculated on O1 or O2 (-0.04851 a.u.), N1 (-0.03486 a.u.), O3 (-0.02975 a.u.) and S1 (-0.01935 a.u.) atoms, respectively.

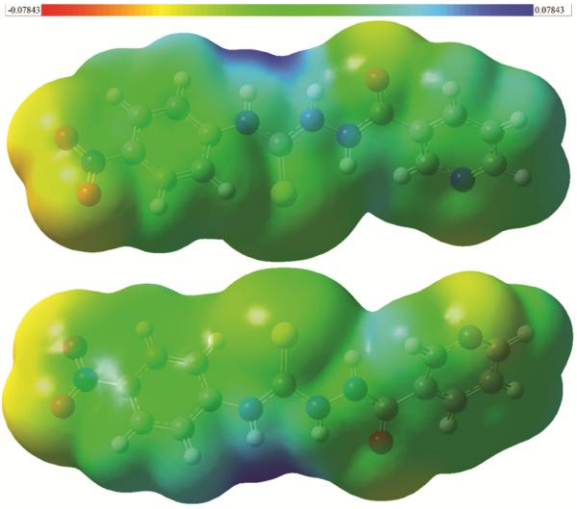

Figure 7 — The MEP surfaces of the compound

Table VII — Calculated the ionization potential (*I*), electron affinity (*A*), electronegativity (÷), chemical hardness (ç), softness (*S*), electrophilicity index (ù), andmaximum charge transfer index (Ä$N_{max.}$) of the compound (T1)

Parameters	Formula	Values
Band gap (eV)	ÄE= | E_{HOMO}-E_{LUMO} |	3.619
Ionization potential (eV)	I=-E_{HOMO}	6.666
Electron affinity (eV)	A=-E_{LUMO}	3.047
Electronegativity (eV)	÷=(I+A)/2	4.857
Hardness (eV)	ç=(I-A)/2	1.810
Softness (eV^{-1})	S=1/2ç	0.276
Electrophilicity index	ù=÷^{2}/2ç	6.517
Max. charge transfer index (eV)	Ä$N_{max.}$= ÷/ç	2.683

Antioxidant properties of thetitle molecule

ABTS$^{\bullet+}$ Radical Scavenging Activity

It is a widely used method based on the removal of the color of the ABTS radical cation, which has a blue-green color, by natural and synthetic compounds and its spectrophotometric measurement. The reaction of this radical with components with antioxidant capacity can be easily determined by measuring the absorbance at 734 nm. ABTS radical cation can be prepared using various oxidizing agents. In this experiment, $K_2S_2O_8$, which is frequently used as an oxidizer, has beenpreferred[67]. The SC_{50} values for the radical scavenging activities of the title compound and standard antioxidant substances have been given in Table VIII ($P< 0.05$). According to the results, the compound does not have an activity as effective as standard antioxidant substances.

DMPD$^{\bullet+}$ Radical Scavenging Activity

The base of this method is the reduction of the dark color of the DMPD radical cation in the presence of a natural or synthetic compound with antioxidant capacity and its spectrophotometric measurement. Due to the hydrogen exchange between the DMPD radical cation and the antioxidant component during the reaction, a decrease in the maximum absorbance value of the DMPD radical cation at 505 nm has beenobserved[68]. According to the obtained results, DMPD radical cation activity decreases in the following order: RUT> BHA> TRO> Compound (Figure 8) ($P< 0.05$).

DPPH Radical Scavenging Activity

This method is based on the electron or hydrogen exchange between DPPH radical and a substance with antioxidant capacity. DPPH radical is a diamagnetic molecule with a maximum absorbance value at 517 nm, and it transforms into a yellow DPPH-H molecule with hydrogen or electron from antioxidant substances[69]. According to the obtained results, the activity of the title compound is not as high as standard antioxidant substances (Figure 8). As can be seen in Table VIII, the activities of the title compound and the standard antioxidants have been reduced in terms of SC_{50} value (µg/mL) in the following order: BHA (8.79 ± 0.08) > RUT (18.05 ± 0.12) > TRO (27.56 ± 0.22) > Compound (64.17 ± 0.23) ($P <0.05$).

Drug-likeness analysis

Molinspiration Cheminformatics free online web service has been used to compute molecular properties and bioactivity score of the molecule[70]. These computed parameters have been listed within Table IX. The Lipinski's rule of five[71]is one of the most common methods used to predict drug-likeness property and pharmacological activities of small molecular systems based on their physicochemical properties. In this way, it can be evaluated whether these will be an effective active oral drug or not. Components of the Lipinski's rule of five are (i) *n*–octanol/water partition coefficient (MlogP)≤5, (ii) weight (MW)≤500 g/mol, (iii) number of hydrogen bond donors (HBD)≤5 and (iv) number of hydrogen bond acceptors (HBA)≤10. The milogP, MW, HBD

Table VIII — Comparison of the radical scavenging activities in terms of SC_{50} (µg/mL)

	ABTS	DMPD	DPPH
Compound	98.52 ± 0.09	85.04 ± 0.20	64.17 ± 0.23
BHA	8.26 ± 0.13	14.94 ± 0.17	8.79 ± 0.08
RUT	17.68 ± 0.16	11.42 ± 0.11	18.05 ± 0.12
TRO	4.46 ± 0.17	28.06 ± 0.19	27.56 ± 0.22

Table IX — Molecular properties and Molinspiration bioactivity score of the compound (T1)

Molecular physicochemical properties	
miLogP	0.86
TPSA	111.87 Å^2
natoms	22
Molecular weight (MW)	317.33 g/mol
nON	8
nOHNH	3
nviolations	0
nrotb	6
Molecular volume	258.68 Å^3
Molinspiration bioactivity score	
GPCR ligand	−0.71
Ion channel modulator	−0.64
Kinase inhibitor	−0.55
Nuclear receptor ligand	−1.04
Protease inhibitor	−0.63
Enzyme inhibitor	−0.44

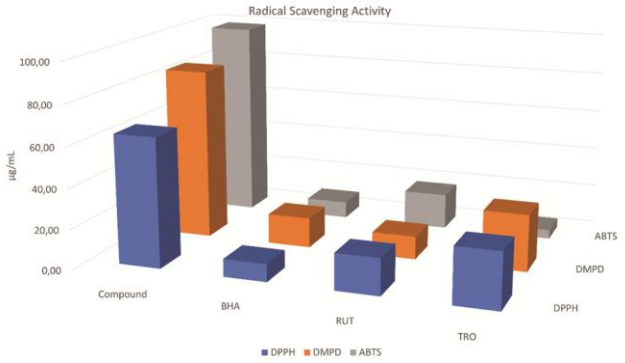

Figure 8 — ABTS, DPMD and DPPH radical scavenging activities of the title compound and standards

(or nOHNH) and HBA (nON) values of the molecule is 0.86, 317.33 g/mol, 3 and 8, respectively. Based on these molecular parameters, this compound can exhibit drug-likeness property in accordance with the Lipinski's rule of five. For the compound, the drug-likeness model score obtained from the Molsoft free website[72] is -0.13. This value indicates that it may be a possible oral drug. Additionally, the TPSA (topological polar surface area) and molecular volume for the compound have been computed as 111.87 $Å^2$ and 258.68 $Å^3$, respectively. Molinspiration bioactivity score parameters have been obtained as -0.71 for GPCR ligand, -0.64 for ion channel modulator, -0.55 for kinase inhibitor, -1.04 for nuclear receptor ligand, -0.63 for protease inhibitor and -0.44 for enzyme inhibitor.

In silico ADMET prediction

The *in silico* ADMET (absorption, distribution, metabolism, excretion and toxicity) predictions have been performed to determine its biological activity by using pharmacokinetic and toxicity properties of the compound. In this context, significant pharmacokinetic and toxicity parameters computed *via* the help of preADMETwebsite[73] have been listed within Table X and Table XI. The value of 100% of the plasma protein binding (PPB) parameter shows that the compound can be transported to other tissues within the body by binding common blood proteins strongly. However, the blood brain barrier (BBB) permeability, which is a barrier for substances that can pass from the blood to the brain, has been computed as 0.021176. This value of the BBB for the compound indicates that it is an inactive compound for the central nervous system (CNS). Namely, this compound under investigation may not be used as a drug that can penetrate the brain. Similarly, it is within a class of moderately absorbed compounds with 86.86393% value of the human intestinal absorption (HIA). The Caco-2 cell permeability and Madin-Darby canine kidney (MDCK) cell parameters have been obtained as 20.398 nm/sec (middle permeability) and 20.7464 nm/sec for the compound, respectively. The other pharmacokinetic properties and some toxicity results obtained for the compound can be seen within Table X and Table XI.

Table X — Pharmacokinetic properties of the compound (T1)

Parameters	Values
In vivo Blood Brain Barrier (BBB) permeability	0.021176
Buffer solubility (mg/L)	2.48593
In vitro Caco-2 cell permeability (nm/sec)	20.398
In vitro CYP2C19 inhibition	Non
In vitro CYP2C9 inhibition	Non
In vitro CYP2D6 inhibition	Non
In vitro CYP2D6 substrate	Non
In vitro CYP3A4 inhibition	Non
In vitro CYP3A4 substrate	Weakly
Human intestinal absorption (HIA)	86.86393%
In vitro Madin-Darby canine kidney (MDCK) (nm/sec)	20.7464
*In vitro*P-glycoprotein (P-gp) inhibition	Inhibitor
In vitro Plasma Protein Binding (PPB)	100%
Pure water solubility (mg/L)	19.4679
In vitro Skin Permeability ($logK_p$, cm/hour)	−4.27159
SKlogD value	1.88427
SKlogP value	1.88427
SKlogS buffer	−5.10601
SKlogS pure	−4.21218

Table XI — Toxicity results of the compound (T1)

Parameters	Values
Acute algae toxicity	0.0520358
Ames test	mutagen
Carcinogenicity (Mouse)	negative
Carcinogenicity (Rat)	positive
Acute daphnia toxicity	0.0536297
In vitro hERG inhibition	Medium risk
Acute fish toxicity (medaka)	0.00658619
Acute fish toxicity (minnow)	0.01360780
Ames TA100 (+S9)	positive
Ames TA100 (−S9)	positive
Ames TA1535 (+S9)	positive
Ames TA1535 (−S9)	negative

Molecular docking study

Molecular docking study has been performed to investigate the nature, species and presence of interactions between SARS-CoV-2 main protease (M^{pro}) and the ligand compound. The high-resolution crystal structure of target macromolecule SARS-CoV-2 M^{pro} protein (PDB ID: 6M0K) has taken from the RCSB Protein Data Bank[74, 75] while the molecular geometry of the ligand compound has been created *via* the experimental SC-XRD study. The AutoDock Vina program has been used for molecular docking procedure[76] while the Discover Studio Visualizer (DSV) one has been used to form .pdb file of the target macromolecule and the ligand compound[77]. Moreover, the DSV program has been used to visualize inter-molecular interactions between the target macromolecule SARS-CoV-2 M^{pro} protein and the ligand compound after the molecular docking procedure.

The active residues that can be within the interaction of any ligand compounds with the target protein are MET6, ALA7, PHE8, GLY15, MET17, TRP31, MET49, ALA70, GLY71, LYS97, GLN127, PHE140, ASN142 GLY143, SER144, CYS145, HIS163, HIS164, MET165, GLU166, HIS172, ASP187, ARG188, GLN189, THR190, GLN192 and ARG298. The dimensional and locational parameters of grid box research docking space within a region containing selected (residues written above as bold and italics) active residues have been set as 36Å×36Å×46Å for volume and (-15.0; 12.0; 68.0) for (center_x; center_y; center_z) at a spacing value of 0.375 Å. The binding affinities and RMSD values computed for ten different poses of the compound docked into the target protein have been given in Table XII. The binding affinity value of -6.90 kcal/mol indicates the best molecular conformational pose docked into the target macromolecule of the ligand compound under investigation. The summary and visualization of the inter-molecular interactions between the ligand and macromolecule corresponding to this pose can be seen in Table XIII and Figure 9, respectively. According to this, eight conventional hydrogen bonds, two carbon-hydrogen bonds, one

Table XII — AutoDock Vina results for different binding poses of the ligand compound (T1) docked into the target macromolecule of PDB ID: 6M0K SARS-CoV-2 M^{pro}

Mode	Binding affinity (kcal/mol)	Distance from best mode (Å)	
		RMSD l.b.	RMSD u.b.
1	−6.90	0.000	0.000
2	−6.20	2.334	7.756
3	−5.90	8.799	12.049
4	−5.90	1.438	2.025
5	−5.80	4.113	5.485
6	−5.70	2.555	7.170
7	−5.70	2.297	7.361
8	−5.60	4.002	7.582
9	−5.60	3.216	4.000
10	−5.50	14.776	16.570

Table XIII — The species, distances and notations of inter-molecular interactions between the docked ligand compound (T1) and the target macromolecule of PDB ID: 6M0K SARS-CoV-2 M^{pro}

Residue	Ligand	Notation	Distance	Interaction
=O atom in HIS164	-NH group in thiourea group	O···H-N	2.73 Å	Conventional Hydrogen Bond
=O atom in HIS164	-NH group in amide group	O···H-N	3.02 Å	Conventional Hydrogen Bond
-S atom in CYS145	-NH group in thiourea group	S···H-N	2.92 Å	Conventional Hydrogen Bond
-NH group in GLN189	=O atom in nitro group	N-H···O	2.24 Å	Conventional Hydrogen Bond
-NH group in THR190	=O atom in nitro group	N-H···O	1.97 Å	Conventional Hydrogen Bond
-NH group in GLN192	=O atom in nitro group	N-H···O	2.07 Å	Conventional Hydrogen Bond
-OH group in SER144	Aromatic N atom in pyridine ring	O-H···N	2.26 Å	Conventional Hydrogen Bond
-OH group in HIS163	Aromatic N atom in pyridine ring	O-H···N	2.95 Å	Conventional Hydrogen Bond
=O atom in PHE140	Aromatic H atom in pyridine ring	O···H-C	2.36 Å	Carbon Hydrogen Bond
Anionic O^- ion in GLU166	Aromatic H atom in pyridine ring	O^-···H-C	3.00 Å	Carbon Hydrogen Bond
-NH group in GLU166	-NH group in amide group	N-H···H-N	2.58 Å	Unfavorable Donor-Donor
Methyl group in MET165	Delocalized pi electrons in phenyl ring	CH_3···ð	3.94 Å	Pi-Sigma
-S atom in MET165	Delocalized pi electrons in phenyl ring	S···ð	4.49 Å	Pi-Sulfur
-S atom in CYS145	Delocalized pi electrons in pyridine ring	S···ð	4.99 Å	Pi-Sulfur

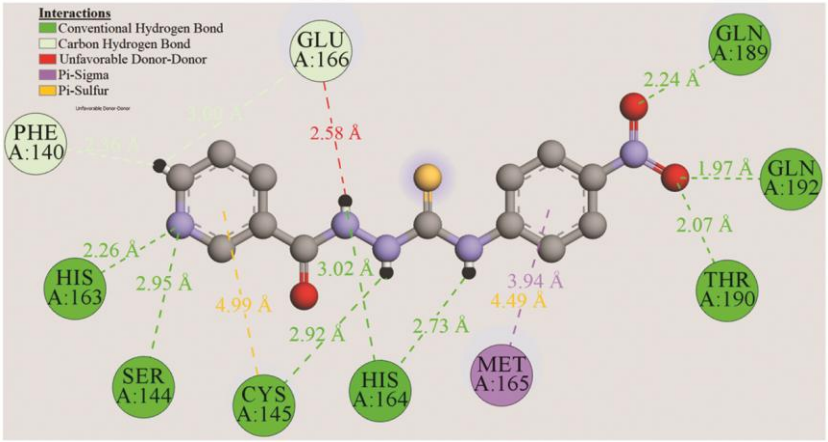

Figure 9 — The interactions between the docked ligand compound and the target macromolecule of PDB ID: 6M0K SARS-CoV-2 M^{pro}

unfavorable donor-donor, one pi-sigma and two pi-sulfur interactions have been detected between the ligand compound and the target macromolecule. Two conventional bond interactions have been found at 2.73 Å (with notation N-H···O) and 2.92 Å (with notation N-H···S) values of interaction distances between -NH groups in thiourea part of the ligand compound with =O atom in residue HIS164 and -S atom in residue CYS145 of the macromolecule. A similar interaction has been obtained at 3.02 Å (with notation N-H···O) between -NH group in thiourea part and =O atom in residue HIS164. There are three inter-molecular O···H-N interactions between =O atoms in nitro group and -NH groups in residues GLN189, THR190 and GLN192, which are at values of 2.24 Å, 1.97 Å and 2.07 Å, respectively. Two conventional hydrogen bond interactions have been formed at 2.26 Å and 2.95 Å with notation N···H-O between pyridine N atom with -OH groups in residues SER144 and HIS163, while two carbon-hydrogen bonds have been obtained at 2.36 Å and 3.00 Å between pyridine hydrogens with =O atom in PHE140 and anionic O^- atom in GLU166, respectively. The other interaction species and distances can be seen in the related table and figure.

Conclusion

The molecular structure and vibrational properties of the compound have been investigated by using X-ray diffractometer and IR spectroscopy experimentally. To compare with experimental values, the quantum mechanical analyses of structural, vibrational and electronic properties of the compound have been performed with the DFT/B3LYP/6-311++G(2d,2p) computational level of theory. For the geometrical and vibrational parameters of the molecule, it can be said that the calculated and observed values are compatible with each other. Six different tautomeric structures of the compound have been optimized for comparison in terms of energies and geometry parameters. The results obtained from the calculations support that the molecule is in thione keto form is the most compatible tautomeric form following the results obtained with X-ray diffraction and IR spectroscopy.

The presence of the intra-molecular $n\rightarrow\pi^*$ and $\pi\rightarrow\pi^*$ electronic transitions has been predicted depending on HOMOs→LUMOs transitions corresponding to the computed UV-Vis. absorption wavelengths. Additionally, some molecular quantum mechanical features have been calculated depending on the HOMO and LUMO energy values. The nucleophilic and electrophilic sites of the molecule have been determined with help of the MEP surface. The most positive electrostatic potential value has been calculated as +0.07843 a.u. for the H4 proton, while the most negative electrostatic potential has been calculated as -0.04851 a.u. for O1 or O2 atoms.

Based on the obtained radical scavenging activity results, it can be said that the title compound has significant, if not very effective, biochemical activity. Thanks to this feature, various *in vitro* and *in vivo* tests are performed and it can be used as an exogenous source for various purposes, such as medical, pharmaceutic, cosmetic, food, *etc*. In the synthesis studies to be carried out in future studies, the existing biochemical activity can be increased by minor reactions on the title compound.

The drug-likeness results of the compound exhibit a possible oral drug property, where *in silico* ADMET results indicate its weak bioactivity. The binding value of -6.90 kcal/mol into the target macromolecule of the compound and its significant intermolecular interaction (especially, eight conventional hydrogen and two carbon-hydrogen bond interactions) with residues within the active site region of the target macromolecule was determined by the molecular docking study.

X-ray structure information

Crystallographic data for the structure reported in this paper have been deposited with the Cambridge Crystallographic Data Centre as supplementary publication number 2077288. These data are provided free of charge by the joint Cambridge Crystallographic Data Centre and Fachinformationszentrum Karlsruhe Access Structures service www.ccdc.cam.ac.uk/structures.

Conflict of Interest

The authors declare no conflict of interest.

References

1 Ma D, Cui F, Xia D & Wang Y, *Anal Lett*, 35, No 2 (2002) 413.
2 Ma D, Li Y, Ma K, Li J, Chen J, Yan J & Wang Y, *Talanta*, 53 (2001) 937.
3 Ma D-L, Li Y, Lü Q-J &Wang Y-L, *J Chinese Chem Soc*, 48 (2001) 1111.
4 Ma D, Ding G, Wang C, Zhang L & Wang Y, *Anal Lett*, 33, No 12 (2000) 2533.
5 West D X, Padhye S B & Sonawane P B, *Complex Chemistry*, 76 (1991) 1.

6 Scovill J P, Klayman D L & Franchino C F, *J Med Chem*, 25 (1982)1261.
7 Vasoya S L, Paghdar D J, Chovatia P T & Joshi H S, *J Sci Islam Repub Iran*, 16 (2005) 33.
8 Namiecińska E, Sobiesiak M, Małecka M, Guga P, Rozalska B & Budzisz E, *Curr Med Chem*, 26 (2019) 664.
9 Plech T, Wujec M, Siwek A, Kosikowska U & Malm A, *Eur J Med Chem*, 46 (2011) 241.
10 Siwek A, Stefanska J, Dzitko K & Ruszczak A, *J Mol Model*, 18 (2012) 4159.
11 Pishawikar S A & More H N, *Arab J Chem*, 10 (2017) S 2714.
12 Hron R & Jursic B S, *Tetrahedron Lett*, 55 (2014) 1540.
13 Sazeli S, Nath A R, Ahmad M H, Zulkifli N W M, Johan M R, Yehye W A & Voon L H, *RSC Adv*, 11 (2021) 7138.
14 Perković I, Tršinar S, Žanetić J, Kralj M, Martin-Kleiner I, Balzarini J, Hadjipavlou-Litina D, Katsori A M & Zorc B, *J EnzymeInhib Med Chem*, 28 (2013) 601.
15 Rineh A, Mahmoodi N, Mohammad A, Foroumadi A, Sorkhi M & Shafiee A, *Arch Pharm*, 340 (2007) 409.
16 Coyne W E & Cusic J W, *J Med Chem*, 11 (1968) 1158.
17 Jain J, Kumar Y, Stables J & Sinha R, *Med Chem*, 6 (2010) 44.
18 Obata T, *Neurochem Res*, 27 (2002) 263.
19 Song G, Li J, Tian H, Li Y, Hu D, Li Y & Cui Z, *Lett Drug Discov*, 13 (2016) 329.
20 Yamaguchi M U, Silva A P B D, Ueda-Nakamura T, Filho B P D, Silva C C D & Nakamura C V, *Molecules*, 14 (2009) 1796.
21 Wujec M, Kedzierska E, Kusmierz E, Plech T, Wróbel A, Paneth A, Orzelska J, Fidecka S & Paneth P, *Molecules*, 19 (2014) 4745.
22 Wos M, Miazga-Karska M, Kaczor A A, Klimek K, Karczmarzyk Z, Kowalczuk D, Wysocki W, Ginalska G, Urbanczyk-Lipkowska Z, Morawiak M & Pitucha M, *Biomed Pharmacother*, 93 (2017) 1269.
23 Šarkanj B, Molnar M, Čačić M & Gille L, *Food Chem*, 139 (2013) 488.
24 Altalhi A A, Hashem H E, Negm N A, Mohamed E A & Azmy E M, *J Mol Liq*, 333 (2021) Article 115977.
25 Tokalı F S, Taslimi P, Usanmaz H, Karaman M & Şendil K, *J Mol Struct*, 1231 (2021) Article 129666.
26 Abram U, Lang E S & Bonfada E, *J Inorg nad Gen Chem*, 628 (2002) 1873.
27 Tada R, Chavda N & Shah M K, *J Chem Pharm Res*, 3 (2011) 290.
28 Leovac V M, Jevtovi V S, Jovanovic L S & Bogdanovic G A, *J Serb Chem Soc*, 70 (2005) 393.
29 El-Gammal O A, Fouda A E A S & Nabih D M, *J Mol Struct*, 1204 (2020) 127495.
30 Azhari S J, Mlahi M R, Mostafa M M, *Spectrochim Acta - Part A Mol Biomol Spectrosc*, 150 (2015) 949.
31 Saravanan R R, Seshadri S, Gunasekaran S, Mendoza-Meroño R & Garcia-Granda S, *Spectrochim Acta - Part A Mol Biomol Spectrosc*, 121 (2014) 268.
32 Gautam P, Prakash O, Dani R K, Singh N K & Singh R K, *Spectrochim Acta - Part A Mol Biomol Spectrosc*, 132 (2014) 278.
33 Crys Alis PRO 11713846 (Rigaku OD, 2015).
34 Sheldrick G M, *Acta Crystallogr A*, 64 (2008) 112.
35 Sheldrick G M, *Acta Crystallogr C*, 71 (2015) 3.
36 Dolomanov O V, Bourhis L J, Gildea R J, Howard J A K & Puschmann H, *J Appl Crystallogr*, 42 (2009) 339.
37 Macrae C F, Edgington P R, McCabe P, Pidcock E, Shields G P, Taylor R, Towler M & Streek J V D, *J Appl Crystallogr*, 39 (2006) 453.
38 Kaştaş Ç A, Kaştaş G, Güder A, Gür M, Muğlu H & Büyükgüngör O, *J Mol Struct*, 1130 (2017) 623.
39 Gökce H, Alpaslan Y B, Zeyrek C T, Ağar E, Güder A, ÖzdemirN & Alpaslan G, *J Mol Struct*, 1179 (2019) 205.
40 Güder A, Korkmaz H, Gökce H, Alpaslan Y B & Alpaslan G, *Spectrochim Acta - Part A Mol Biomol Spectrosc*, 133 (2014) 378.
41 Frisch M J, Trucks G W, Schlegel H B, Scuseria G E, Robb M A, Cheeseman J R, Scalmani G, Barone V, Mennucci B, Petersson G A, Nakatsuji H, Caricato M, Li X, Hratchian H P, Izmaylov A F, Bloino J, Zheng G, Sonnenberg J L, Hada M, Ehara M, Toyota K, Fukuda R, Hasegawa J, M Ishida, Nakajima T, Honda Y, Kitao O, Nakai H, Vreven T, Montgomery J A, Peralta J E, Ogliaro F, Bearpark M, Heyd J J, Brothers E, Kudin K N, Staroverov V N, Kobayashi R, Normand J, Raghavachari K, Rendell A, Burant J C, Iyengar S S, Tomasi J, Cossi M, Rega N, Millam J M, Klene M, Knox J E, Cross J B, Bakken V, Adamo C, Jaramillo J, Gomperts R, Stratmann R E, Yazyev O, Austin A J, Cammi R, Pomelli C, Ochterski J W, Martin R L, Morokuma K, Zakrzewski V G, Voth G A, Salvador P, Dannenberg J J, Dapprich S, Daniels A D, Farkas Ö, Foresman J B, Ortiz J V, Cioslowski J & Fox D J, *Gaussian 09*, Revision C01, 9, (Gaussian Inc, Wallingford CT) 2009.
42 Dennington R, Keith T & Millam J, *Gauss View*, Version 5, (Semichem Inc, Shawnee Mission K S) 2009.
43 Becke A D, *J Chem Phys*, 98 (1993) 5648.
44 Lee C, Yang W & Parr R G, *Phys Rev B*,37 (1998) 785.
45 Jamróz M H, *Vibrational Energy Distribution Analysis VEDA 4*, (Warsaw) 2004.
46 Runge E & Gross E K U, *Phys Rev Lett*, 52 (1984) 997.
47 Trott O & Olson A J, *J Comput Chem*, 31 (2010) 455.
48 Colthup N B, Daly L H & Wiberley S E, *Introduction to Infrared and Raman Spectroscopy*, (Academic Press, New York) 1964.
49 Bellamy L J, *The Infrared Spectra of Complex Molecules*, 3rd edn, (John Wiley & Sons, New York) 1975.
50 Stuart B H, *Infrared Spectroscopy: Fundamentals and Applications*, (John Willey & Sons, England) 2004.
51 Silverstein R M, Webster F X & Kiemle D J, *Spectroscopic identification of organic compound*, 7th edn, (John Wiley & Sons, USA) 2005.
52 Alaşalvar C, Öztürk N, Abdel-Aziz A A-M, Gökce H, El-Azab A S, El-Gendy M A & Sert Y, *J Mol Struct*, 1171 (2018) 696.
53 Öztürk N & Gökce H, *J Appl Spect*, 86 (2019) 138.
54 Öztürk N, *J Mol Struct*, 1193 (2019) 468.
55 Abosadiya H M, Hasbullah S A & Yamin B M, *Spectrochim Acta A Mol Biomol Spectrosc*, 144 (2015) 115.
56 Mushtaque M, Jahan M, Ali M, Khan M S, Khan M S, Sahay P & Kesarwani A, *J Mol Struct*, 1122 (2016) 164.
57 Sathiya S, Senthilkumar M & Raja C R, *J Mol Struct*, 1180 (2019) 81.
58 Fatima S, Sharma R, Asghar F, KamalA, Badshah A & Kraatz H B, *J Ind Eng Chem*, 76 (2019) 374.

59 Sert Y, Karakaya M, Çırak Ç, Eskiyurt B & Kürekçi M, *J Sulphur Chem*, 36 (2015) 450
60 Sert Y & Ucun F, *Indian J Phys*, 87 (2013) 809.
61 Ceylan Ü, Tarı G Ö, Gökce H & Ağar E, *J Mol Struct*, 1110 (2016) 1.
62 Gökce H, Alpaslan Y B, Zeyrek C T, Ağar E, Güder A, Özdemir N & Alpaslan G, *J Mol Struct*, 1179 (2019) 205.
63 O'boyle N M, Tenderholt A L & Langner K M, *J Comput Chem*, 29 (2008) 839.
64 Fukui K, *Science*, 218 (1982) 747.
65 Gökce H, Öztürk N, Ceylan Ü, Alpaslan Y B & Alpaslan G, *Spectrochim Acta A Mol Biomol Spectrosc*, 163 (2016) 170.
66 Öztürk N, Gökce H, *Bilgesci*, 1 (2017) 9.
67 Alaşalvar C, Soylu M S, Güder A, Albayrak Ç, Apaydın G & Dilek N, *Spectrochim Acta A Mol Biomol Spectrosc*, 130 (2014) 357.
68 Güder A, *Iran J Pharm Sci*, 15 (2016) 301.
69 Gür M, Muğlu H, Çavus M S, Güder A, Sayıner H S & Kandemirli F, *J Mol Struct*, 1134 (2017) 40.
70 MolinspirationCheminformatics, https://wwwmolinspirationcom/ (Access: 15 May 2021).
71 Lipinski C A, I,ombardo F, Dominy B W & Feeney P J, *Adv Drug Deliv Rev*, 23 (1997) 3.
72 Molsoft https://molsoftcom/indexhtml (Access: 15 May 2021).
73 Pre ADMET, https://preadmetbmdrckr/ (Access: 15 May 2021).
74 RCSB Protein Data Bank (PDB), http://wwwrcsborg (Access: 15 May 2021).
75 Jin Z, Du X, Xu Y, Deng Y, Liu M, Zhao Y, Zhang B, Li X, Zhang L, Peng C, Duan Y, Yu J, Wang L, Yang K, Liu F, Jiang R, Yang X, You T, Liu X, Yang X, Bai F, Liu H, Liu X, Guddat L W, Xu W, Xiao G, Qin C, Shi Z, Jiang H, Rao Z & Yang H, *Nature*, 582 (2020) 289.
76 Trott O & Olson A J, *J Comput Chem*, 31 (2010) 455.
77 Dassault Systèmes BIOVIA, *DS Visualizer 2019*, (San Diego, Dassault Systèmes) 2019.